Article

Fabrication of a Heterobinuclear Redox Cycle to Enhance the Photocatalytic Activity of BiOCl

Dongmei Li *, Guisheng Liu, Xiaojie Li, Zhuo Gao, Hangqi Shao and Zhongzhen Tian

Inner Mongolia Key Laboratory of Coal Chemical Engineering & Comprehensive Utilization, School of Chemistry and Chemical Engineering, Inner Mongolia University of Science & Technology, Baotou 014010, China; liugugumi@163.com (G.L.); lixiaojie01142022@163.com (X.L.); gz483781532@sina.com (Z.G.); imust1999@163.com (H.S.); 2019952@imust.edu.cn (Z.T.)
* Correspondence: 2019951@imust.edu.cn; Tel.: +86-150-4740-5248

Abstract: La^{3+} and Ni^{2+}-doped BiOCl were prepared by sol–gel method and characterized by physicochemical and spectroscopic techniques. Their photocatalytic performances were investigated by the degradation of gentian violet under visible light. The results indicated that the co-doping of Ni and La significantly enhanced the photocatalytic performance of BiOCl. The photodegradation efficiency of LaNiBiOCl reached 95.5% in 105 min, which was 1.5 times that of BiOCl. This significant enhancement in photocatalytic activity was mainly attributed to the effective capture and transfer of photogenerated electrons between heterobinuclear La and Ni redox cycle, which benefited the photodegradation of active h^+ and the formation of active $\bullet O_2^-$. Furthermore, the photodegradation activity did not show an obvious drop after five recycles, indicating that LaNiBiOCl was a promising semiconductor photocatalyst for the degradation of gentian violet.

Keywords: BiOCl; doping; gentian violet; photodegradation

1. Introduction

Photocatalysis, which can deeply and non-selectively oxidize all kinds of organic molecules, has become a promising technique for wastewater treatment due to its energy savings and environmental friendliness [1,2]. At the same time, photocatalysts are crucial to achieving an excellent photocatalytic degradation effect. In recent years, Bismuth oxychlorides [3–7] have been extensively studied as photocatalysts. Especially, BiOCl [8–11] has shown remarkable photodegradation activity and practical application potential due to its layered structure, suitable bandgap, low cost, non-toxicity, and high chemical and optical stability [12–14]. However, the relatively wide bandgap and high recombination rate of photogenerated carriers of BiOCl hinder its practical application.

Many methods have been used to solve these shortcomings, such as heterojunctions [15–18], element doping [19–22], and surface functionalization [23,24]. The doping method includes non-metal ion doping, metal ion doping, and co-doping. In metal ion doping, transition metal ions [25–31] and rare earth ions [32,33] are intensively researched due to their variable valence. It is reported that the replacement of Bi^{3+} by Ni^{2+} will cause structure distortion due to the smaller radius of Ni^{2+} (69 pm) compared to that of Bi^{3+} (103 pm) and result in the formation of oxygen vacancies, which facilitate the capture of e^- by adsorbed O_2 to form highly active $\bullet O_2^-$ [34]. The band gap of BiOCl is adjusted by the impurity energy level formed by doping ions and thus broadens its photoresponse range [28]. On the other hand, rare earth metal ions are usually introduced to serve as electron or hole traps and thus inhibit photogenerated electron–hole pair recombination. It is reported that when Bi^{3+} is replaced by La^{3+}, abundant surface hydroxyls are generated, and thus the adsorption of dye is improved [35]; La^{3+} sites also serve as photogenerated electron traps [35,36]. As for co-doping, different rare earth metal ions co-doping are mainly involved [37,38]. In this case, the co-doping of transition metal ions and rare earth metal

ions only involves Fe and Nd co-doping [39], in which the Fe lowers the band gap energy and Nb acts as an electron trap. The cooperative effects of Fe and Nb lead to improved visible-light photocatalytic activity.

Thus, in this work, a La and Ni co-doped BiOCl photocatalyst is prepared. The co-doping of Ni^{2+} and La^{3+} makes the introduced impurity level closer to the valence band of BiOCl, improving the utilization of visible light. At the same time, La^{3+} acts as a scavenger of photogenerated electrons to improve the photocatalytic efficiency of active h^+, while Ni^{2+} promotes the adsorption of substrates and the formation of active species $\bullet O_2^-$; the synergy effects of La^{3+} and Ni^{2+} will greatly improve the visible-light-driven photocatalytic degradation efficiency of BiOCl.

2. Results and Discussion

2.1. Structure and Composition

The XRD patterns of as-prepared BiOCl, NiBiOCl, LaBiOCl, and LaNiBiOCl were shown in Figure 1. The diffraction peaks of BiOCl (at 2θ = 24.16°, 25.88°, 32.56°, 33.52°, 36.72°, 40.9°, 46.76°, 49.84°, 55.16°, 58.68°) could be ascribed to (002), (101), (110), (102), (003), (112), (200), (113), (104), and (212) crystal planes, which were in good accordance with standard card (JCPDS No. 06-0249), indicating its tetragonal crystal structure [40]. NiBiOCl, LaBiOCl, and LaNiBiOCl gave similar diffraction peaks to those of pure BiOCl, but the peak intensities increased after doping Ni and/or La, indicating that Ni and La had a positive effect on the crystallization of BiOCl [28]. Especially, the diffraction intensities of the (101) crystal plane in LaBiOCl and LaNiBiOCl increased significantly, suggesting that BiOCl might grow preferentially toward this plane after La doping. Moreover, the peak center shifted to a higher 2θ ($\Delta\theta$ = 0.08 for (101) crystal plane) after Ni doping due to the smaller radius of Ni^{2+} (69 pm) compared to that of Bi^{3+} (103 pm), which caused the lattice shrinkage [41]. The shift also confirmed the successful substitution of Ni^{2+} for Bi^{3+}. Meanwhile, no obvious peak center shift was observed after doping of La because of their equivalent radius of Bi^{3+} and La^{3+} (101 pm). The diffraction peaks of Ni, La, and other elements were not observed, indicating the higher purity of the as-prepared photocatalysts.
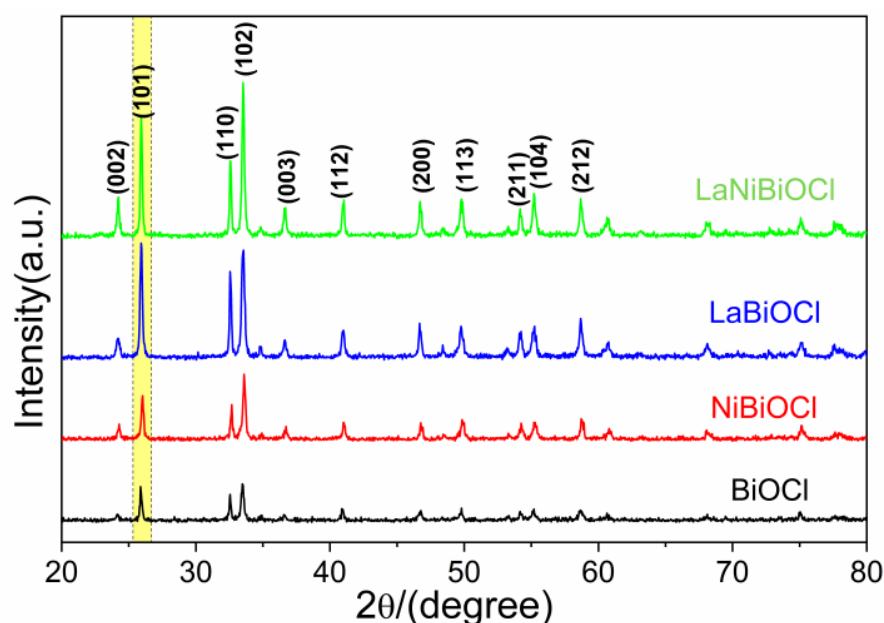

Figure 1. XRD patterns of as-prepared samples.

The surface functional groups of prepared samples were analyzed by the FT-IR method (Figure 2). The bands centered at 3420 cm^{-1} and 1640 cm^{-1} could be assigned to the O-H stretching vibration of surface hydroxyl and H-O-H bending vibration of water adsorbed

on the surface, respectively, which could generate hydroxyl radicals under irradiation [42]. The bands at 2800–2930 cm^{-1} were ascribed to the symmetric and antisymmetric stretching vibration of -CH$_2$- since ethanol was used as a solvent in the preparation process [43]. The characteristic Bi-O vibration shifted from 528 cm^{-1} in BiOCl to 526 cm^{-1} after Ni and/or La doping, indicating the component change of the photocatalysts [44].
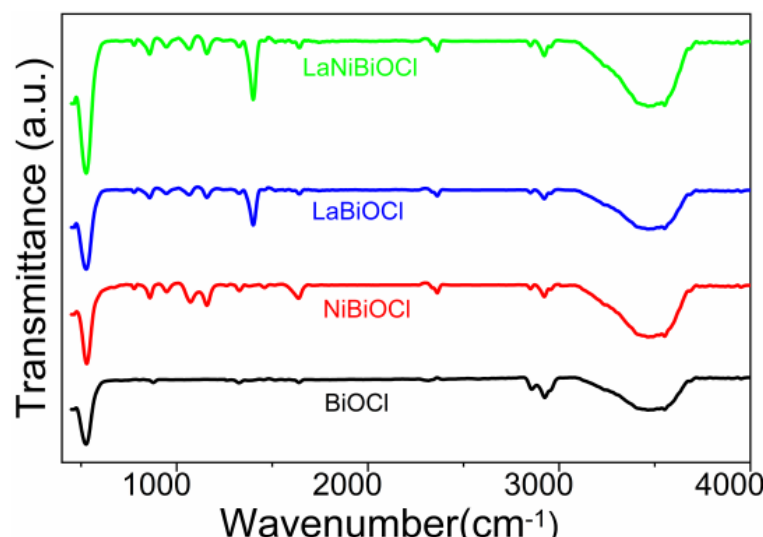

Figure 2. FT–IR spectra of as-prepared samples.

The chemical state of surface elements and the effect of doping on the coordination environment were further analyzed by the XPS method (Figure 3). Bi, Cl, and O were observed in all samples (Figure 3a). However, Ni and La were not observed in a survey and high-resolution scan of NiBiOCl, LaBiOCl, and LaNiBiOCl, which might be due to the low doping amount of Ni (2‰) and La (2‰). The high-resolution Bi 4f spectra are shown in Figure 3b. For BiOCl, two characteristic peaks at 159.55 eV and 164.85 eV could be ascribed to Bi 4f$_{7/2}$ and Bi 4f$_{5/2}$, indicating the existence of Bi^{3+} [45,46]. The spacing of the two peaks was 5.3 eV, indicating the normal state of Bi in BiOCl [47]. After doping of Ni and/or La, these two peaks shifted to a lower position because of the increase in the electron density of Bi, which was the result of an increase in oxygen defects formed from the substitution of Bi by Ni or/and La. The high-resolution Cl 2p (Figure 3c) of BiOCl showed two peaks at 199.85 eV and 198.2 eV, which were ascribed to Cl 2p$_{1/2}$ and Cl 2p$_{3/2}$, respectively. For high-resolution O 1s spectra (Figure 3d), multiple chemical states were observed in NiBiOCl, LaBiOCl, and LaNiBiOCl. The peaks at about 530 and 532 eV were ascribed to lattice oxygen and oxygen defects [48]. The binding energy of the oxygen defect of LaNiBiOCl shifted 0.38 eV to the lower direction, while the corresponding shifts for NiBiOCl and LaBiOCl were 0.2 and 0.1 eV, respectively. This result suggested that there were more defects or water adsorbed on the surface of LaNiBiOCl, which was beneficial to improving its photodegradability.
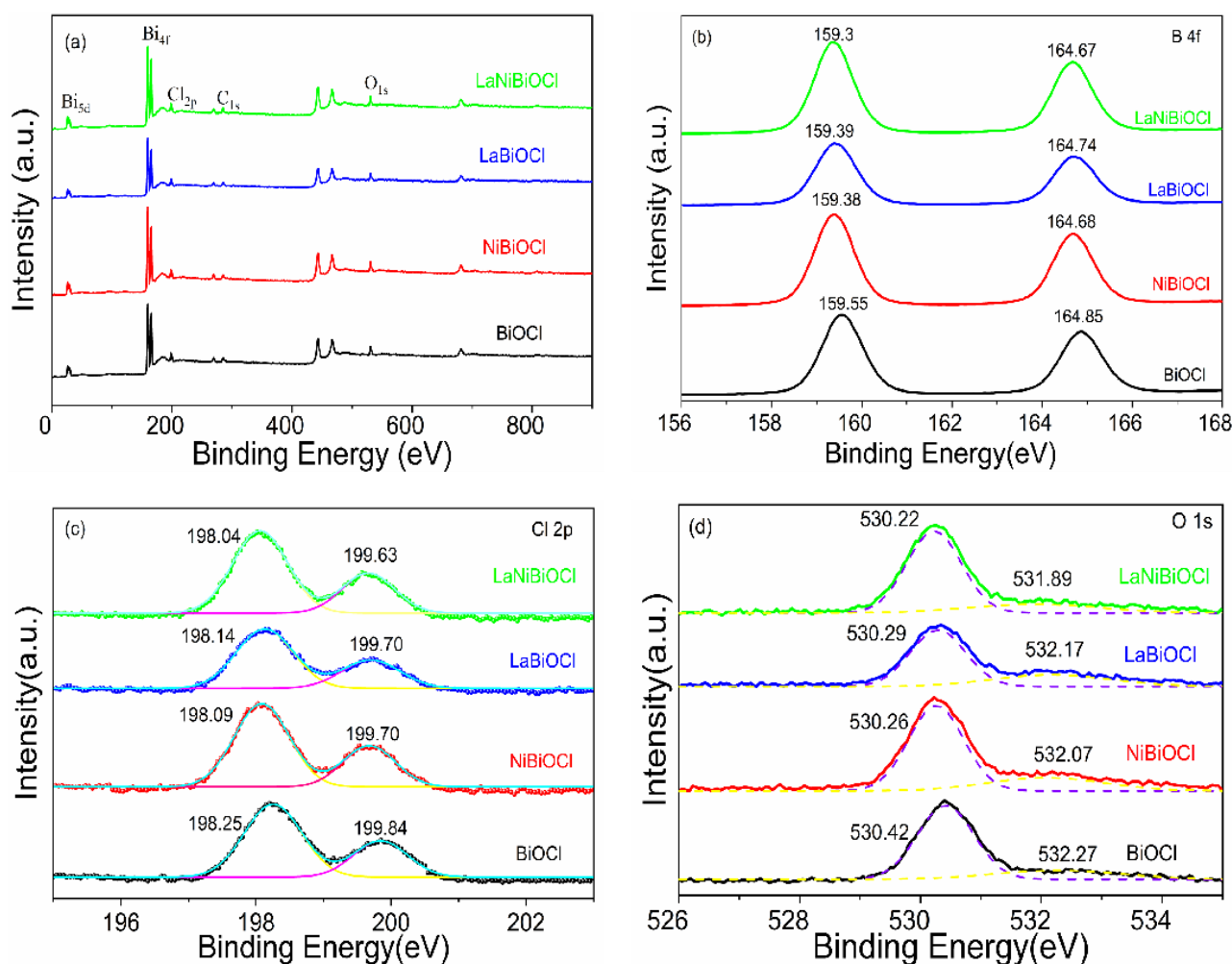
Figure 3. XPS survey and corresponding high-resolution spectra of as-prepared samples. (**a**) Survey spectra (**b**) Bi 4f, (**c**) Cl 2p, and (**d**) O 1s.

2.2. Morphology and Microstructure

The morphology and microstructure of as-prepared photocatalysts were characterized by SEM and TEM. It can be seen in Figure 4a–d that all samples consisted of numerous nanoflakes [49] 0.1–1 um in diameter and 20 nm in thickness. There was no apparent change in morphology after Ni and/or La doping. These ultra-thin nanoflakes had a huge surface area and higher surface energy, so they easily aggregated together. Additionally, mesopores or macropores could be formed during the aggregating process, so the diffusion resistance of the gentian violet molecules in these pores was very small, and it was easier for gentian violet to contact and react with the active sites on the surface of the prepared photocatalysts. These meso–macro pores and square nanoflake structures of LaNiBiOCl were more obvious in TEM (Figure 4e–f). The element mapping of LaNiBiOCl (Figure 4g–h) confirmed the uniform distribution of La and Ni in the photocatalyst, indicating that the doping of Ni and La was successful.
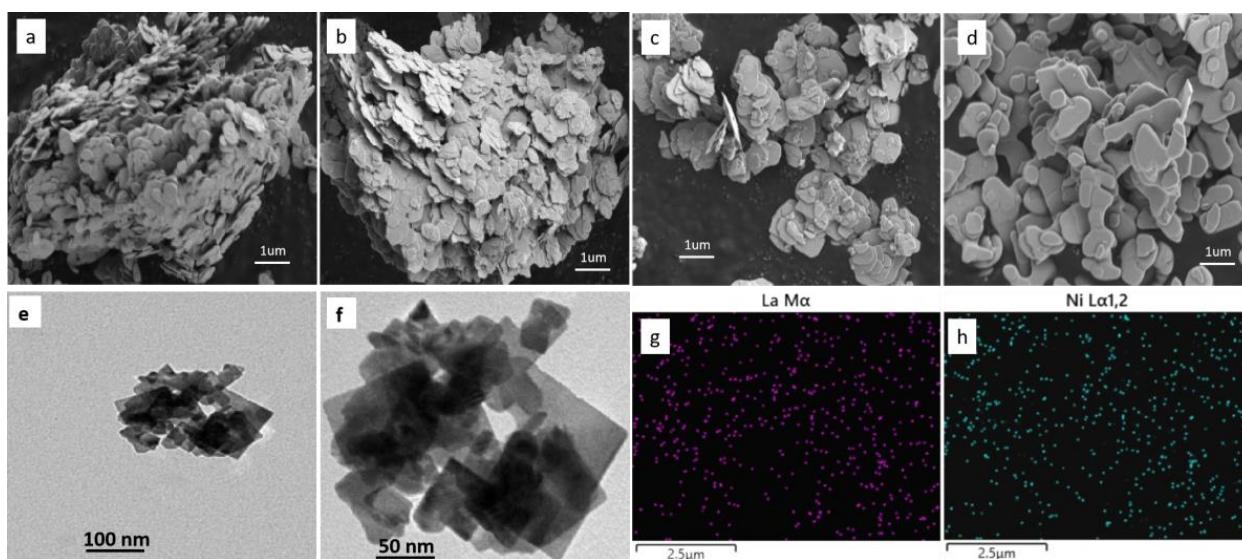
Figure 4. SEM micrographs of as-prepared photocatalysts: BiOCl (**a**), NiBiOCl (**b**), LaBiOCl (**c**), and LaNiBiOCl (**d**); TEM of LaNiBiOCl (**e,f**); and EDS of La and Ni in LaNiBiOCl (**g,h**).

2.3. Optical and Electrical Properties

UV-Vis spectroscopy was used to evaluate the light utilization of the photocatalyst. It can be seen in Figure 5 that the absorption edge shifted slightly to red after doping, and the absorption in the visible region was greatly improved for LaBiOCl and LaNiBiOCl. The band gap values estimated from the diffuse reflectance spectra were 3.38, 3.31, 3.24, and 3.22 eV for BiOCl, NiBiOCl, LaBiOCl, and LaNiBiOCl, respectively. The conduction band (CB) minimum of BiOCl was occupied by Bi 6p, while the valence band (VB) maximum was composed of O 2p and Cl 3p. When Bi^{3+} was replaced by Ni^{2+} and/or La^{3+}, the CB decreased; when the surface oxygen vacancies increased the VB width, these two aspects led to a decrease in the band gap of BiOCl [32].
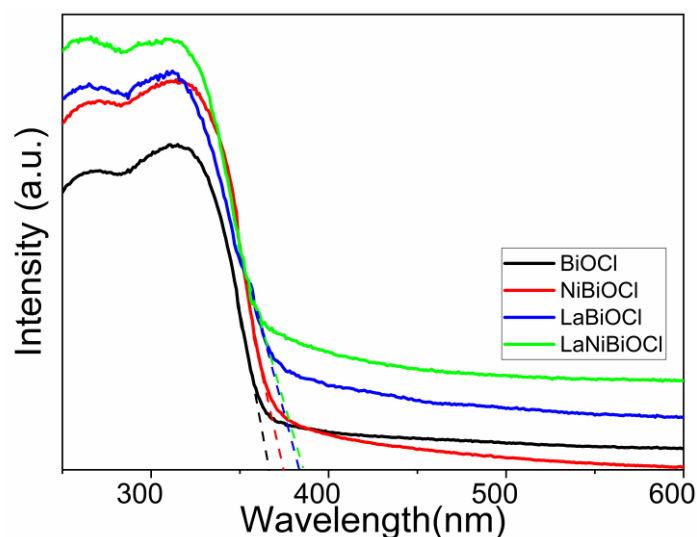
Figure 5. UV-Vis absorption spectra of as-prepared samples.

PL was used to investigate the recombination efficiency of photogenerated electrons and holes [50,51]. The PL (Figure 6a) intensities at 470 nm were in the following order: BiOCl > NiBiOCl > LaBiOCl > LaNiBiOCl. A weaker PL intensity suggested a higher efficiency of photogenerated electron–hole separation. Thus, LaNiBiOCl was better than the others in terms of photogenerated carrier separation, resulting in higher photocatalytic ac-

tivity. The oxygen vacancies formed by Ni and/or La doping could capture photoelectrons and thus promote the separation of photogenerated electrons and holes.

EIS was another valid strategy to measure the separation and transfer efficiency of photogenerated electrons and holes. Generally, the smaller the EIS arc radius, the higher the separation efficiency of photogenerated carriers and the faster the interfacial charge transfer. It could be seen from Figure 6b that the semicircle arcs were in the order BiOCl > NiBiOCl > LaBiOCl > LaNiBiOCl, indicating the highest separation efficiency and fastest interfacial charge transfer in LaNiBiOCl.
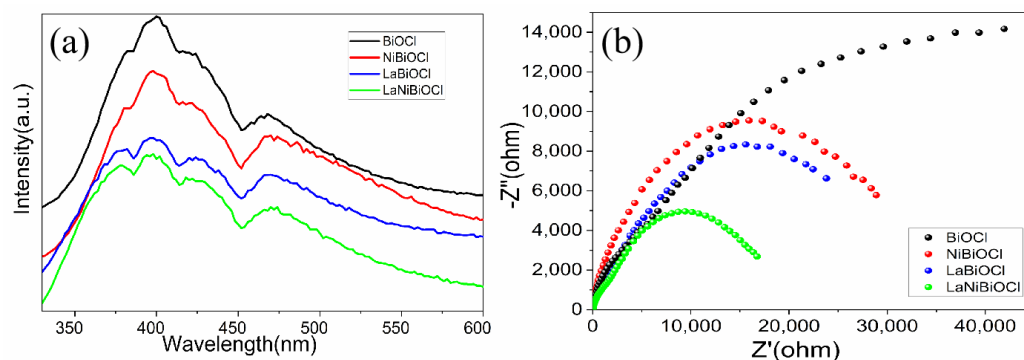

Figure 6. PL spectra (**a**) λ_{ex} = 310 nm and EIS (**b**) of as-prepared samples.

2.4. Photocatalytic Activity

The photocatalytic activities of as-prepared samples were evaluated by the degradation of gentian violet under simulated visible light (Figure 7). It is well known that photocatalytic reactions occur at the surface of photocatalysts [52,53], so it was very important for the substrate to be adsorbed to the surface of photocatalysts. The adsorption behaviors of as-prepared samples were investigated by dark adsorption experiments (Figure 7a). It was obvious that the initial adsorption of gentian violet was very rapid in NiBiOCl and LaNiBiOCl. After about 40 minitues, adsorption–desorption equilibriums were almost achieved for all the as-prepared samples. Figure 7b shows the visible-light activities of the as-prepared samples in the degradation of gentian violet. It was obvious that doped photocatalysts showed better catalytic activities than that of BiOCl. The photodegradation percentages of gentian violet after 105 min irradiation were 63.2%, 76.1%, 89.6%, and 95.5% for BiOCl, NiBiOCl, LaBiOCl, and LaNiBiOCl, respectively. The degradation efficiency of LaNiBiOCl was 1.5 times higher than that of BiOCl. The linear kinetics modeling results of as-prepared samples (Figure 7c) indicated that the degradation of gentian violet on these photocatalysts followed a first-order kinetic [54]. The kinetic constants for BiOCl, NiBiOCl, LaBiOCl, and LaNiBiOCl were 0.01042, 0.01561, 0.02235, and 0.03056 min^{-1}, respectively, indicating that LaNiBiOCl displayed the highest conversion rate.

There were various photoinduced active species, such as holes (h$^+$), hydroxyl radical (•OH), and superoxide radical (•O$_2^-$), which were directly involved in the photocatalytic degradation process [55]. To detect the active species, ammonium oxalate (AO), isopropyl alcohol (IPA), and 1,4-benzoquinone (BQ) were used, respectively, as scavengers of h$^+$, •OH, and •O$_2^-$ [56,57]. Figure 7d demonstrates that the highly active h$^+$ (the oxidation potential of h$^+$ is 3.0 V) played a dominant role and •O$_2^-$ exerted a secondary role in the photocatalytic degradation process of gentian violet in all as-prepared catalysts [58], while the impact of •O$_2^-$ in NiBiOCl was larger than that in LaBiOCl. According to this, a degradation mechanism (Figure 7e) of gentian violet on LaNiBiOCl was proposed. The amine nitrogen in the gentian violet structure could form an O-M-O bond with Ni or La in the LaNiBiOCl catalyst and thus adsorb onto its surface. The dark adsorption experiment in Figure 7a displayed that LaNiBiOCl had the highest adsorption capacity for gentian violet, so these adsorbed gentian violets would act as a photosensitizer for LaNiBiOCl. When gentian violet absorbed 450–600 nm light and formed an excited state, the photogenerated

electrons transferred from the LUMO energy level of gentian violets to the conduction band of LaNiBiOCl, and then the oxygen molecules adsorbed on the surface of LaNiBiOCl trapped these electrons to generate $\bullet O_2^-$. On the other hand, the photosensitization of gentian violet could rapidly accelerate the Ni^{3+}/Ni^{2+}-La^{3+}/La^{2+} cycling process [59]. At the same time, the photogenerated h^+ could also directly oxidize gentian violet.

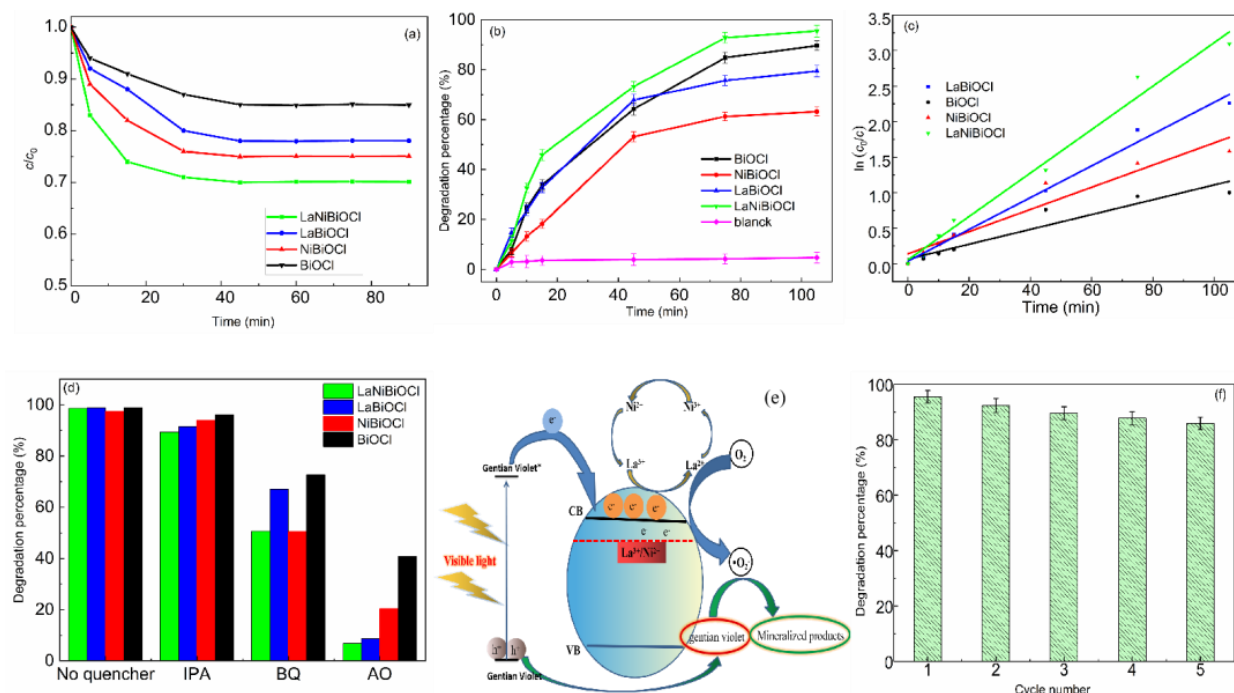**Figure 7.** The dark adsorption curves (**a**), degradation curves (**b**), linear kinetics curves (**c**), and quenchers tests (**d**) of four as−prepared samples. Cycling test (**e**) and band structure model (**f**) of LaNiBiOCl.

Stability was another important factor in evaluating the application of the photocatalyst. Figure 7f shows the stability of LaNiBiOCl after five recycles of photodegradation. The degradation percentage of the fifth cycle was 85.9%, which was a 10% decrease compared with the initial one (95,5%); this decrease was partially related to the loss of LaNiBiOCl during the recycling experiment. Thus, LaNiBiOCl exhibited very good stability.

3. Materials and Methods

3.1. Preparation of Photocatalysts

Firstly, Bi_2O_3 and La_2O_3 were dissolved, respectively, in 30 mL of concentrated hydrochloric acid and then heated to remove the residual concentrated hydrochloric acid. Secondly, 15 mL of deionized water and 10 mL of ethanol were added to the as-prepared $BiCl_3$ solution under magnetic stirring. Then, as-prepared $LaCl_3$ and/or $NiCl_2$ was added with the ratio n(La):n(Ni):n(Bi) = 1:1:500. The pH of the solution was adjusted to 2~3 with ammonia, and white flocculent precipitate appeared. Then, the mixture was placed in an oil bath at 80 °C for 20 h. Afterward, the suspension was centrifuged and washed three times with deionized water. The obtained solid was dried at 120 °C to obtain LaNiBiOCl, NiBiOC, or LaBiOCl. For comparison, the pure BiOCl was also prepared by the same method without adding La and Ni.

3.2. Characterization

The phase and crystal structure of obtained samples were characterized using a D8 advanced X-ray diffractor (Bruker AXS Company, Fitchburg, WI, USA) with Cu Ka radiation. The Fourier transform infrared (FT−IR) spectra were conducted on a BRUKER

VERTEX70 spectrometer (Bruker Company, Madison, WI, USA). X-ray photoelectron spectroscopy (XPS) data were collected on an ESCALAB 250 XL device (Thermo Fisher Scientific, Waltham, MA, USA). The morphologies and compositions of as-prepared samples were obtained by scanning electron microscopy (SEM, S-2500, Oxford Instruments, Oxford, UK) and transmission electron microscopy (TEM, JEOL-1400, JEOL, Tokyo, Japan). UV-Vis diffuse reflectance spectra were recorded using a UV-2550 spectrophotometer (Shimadzu, Kyushu, Japan). Photoluminescence (PL) spectra were obtained on an Edinburgh Instruments FLS920 fluorescence spectrometer (Edinburgh Instruments Ltd., Livingston, UK). Electrochemical impedance spectroscopy (EIS) was measured on an electrochemical workstation (CHI 760E, CH Instrument Co. Ltd., Shanghai, China). Platinum and saturated Ag/AgCl were used as the counter electrode and reference electrode, respectively.

3.3. Photocatalytic Activity Experiment and Stability Test

Gentian violet was applied to investigate the photocatalytic activity of the obtained photocatalysts. In these experiments, a 400 W Xenon lamp equipped with a 420 nm cut-off filter was engaged as visible light source. Typically, 0.5 g of as-prepared photocatalyst was dispersed in 50 mL of gentian violet aqueous solution (20 mg/L). Before light irradiation, the suspension was maintained in the dark for 45 min under continuous magnetic stirring. Afterward, the suspension was exposed to visible light under magnetic stirring. At 30 min intervals, 3 mL of suspension was taken out and filtered by a 0.45 μm membrane filter, and the concentration of gentian violet in the supernatant was measured by a UV-Vis spectrophotometer.

Additionally, recycling tests were conducted to investigate the reusability and stability of LaNiBiOCl. After each photocatalytic reaction, LaNiBiOCl was collected by centrifugation, washed thoroughly with deionized water and anhydrous alcohol, and then dried in vacuum at 60 °C. Subsequently, the reclaimed LaNiBiOCl was put into the fresh gentian violet solution for the next photocatalytic experiment. This test was repeated five times.

4. Conclusions

In summary, La and/or Ni-doped BiOCl were successfully prepared by the sol–gel method. XRD analysis disclosed their tetragonal phase. The bandgap of BiOCl declined after doping; the results of PL and EIS demonstrated that the La and Ni co-doped BiOCl effectively enhanced the transfer and separation of photogenerated electrons and holes. The mechanism might be a photosensitization process, and the injected electrons were captured by La^{3+} and then transferred in the heterobinuclear redox cycle of La and Ni, which prolonged the recombination time of photogenerated carriers and thus improved the photodegradation efficiency of the main active species, h^+. Moreover, the captured electrons could be faster and easily transferred to adsorbed oxygen molecules to form the secondary intermediate active species $\bullet O_2^-$. Therefore, the Ni and La co-doped BiOCl exhibited the best catalytic performance with a catalytic degradation efficiency of 95.5% in 105 min.

Author Contributions: Z.T. conceived and designed the experiments; G.L. and H.S. participated in the experiments and measurements; D.L. drafted the manuscript; X.L. responded to reviewers; Z.G. conducted supplementary experiments during the manuscript's revision process. All authors have read and agreed to the published version of the manuscript.

Data Availability Statement: Not applicable.

References

1. Hassan, N.S.; Jalil, A.A. A review on self-modification of zirconium dioxide nanocatalysts with enhanced visible-light-driven photodegradation of organic pollutants. *J. Hazard. Mater.* **2022**, *423*, 126996. [CrossRef] [PubMed]
2. Li, C.Y.; Wang, B.Q.; Zhang, F.J.; Song, N.N.; Liu, G.; Wang, C.; Zhong, S. Performance of Ag/BiOBr/GO composite photocatalyst for visible-light-driven dye pollutants degradation. *J. Mater. Res. Technol.* **2020**, *9*, 610–621. [CrossRef]
3. Xu, H.Y.; Han, X.; Tan, Q.; He, X.L.; Qi, S.Y. Structure-dependent photocatalytic performance of BiOBrxI1-x nanoplate solid solutions. *Catalysts* **2017**, *7*, 153. [CrossRef]
4. Arthur, R.B.; Ahern, J.C.; Patterson, H.H. Application of BiOX photocatalysts in remediation of persistent organic pollutants. *Catalysts* **2018**, *8*, 604. [CrossRef]
5. Zhang, B.K.; Fu, S.W.; Wang, D.B.; Jiao, S.J.; Zeng, Z.; Zhang, X.Y.; Xu, Z.K.; Liu, Y.X.; Zhao, C.C.; Pan, J.W.; et al. Synthesis an enhanced light photocatalytic activity of modulating band BiOBr$_x$I$_{1-x}$ nanosheets. *Nanomaterials* **2021**, *11*, 2940. [CrossRef]
6. Cui, B.Y.; Cui, H.T.; Li, Z.R.; Dong, H.Y.; Li, X.; Zhao, L.F.; Wang, J.W. Novel Bi$_3$O$_5$I$_2$ hollow microsphere and its enhanced photocatalytic activity. *Catalysts* **2019**, *9*, 709. [CrossRef]
7. Zeng, Q.D.; Xie, W.; Chen, Z.H.; Wang, X.; Akinoglu, E.M.; Zhou, G.F.; Shui, L.L. Influence of the facets of Bi$_{24}$O$_{31}$Br$_{10}$ naobelts and nanosheets on theire photocatalytic properties. *Catalysts* **2020**, *10*, 257. [CrossRef]
8. Ganose, A.M.; Cuff, M.; Butler, K.T.; Walsh, A.; Scanlon, D.O. Interplay of orbital and relativistic effects in bismuth oxyhalides: BiOF, BiOCl, BiOBr, and BiOI. *Chem Mater* **2016**, *28*, 1980–1984. [CrossRef]
9. Li, J.; Yu, Y.; Zhang, L. Bismuth oxyhalide nanomaterials: Layered structures meet photocatalysis. *Nanoscale* **2014**, *6*, 8473–8488. [CrossRef]
10. Cheng, H.; Huang, B.; Dai, Y. Engineering BiO$_X$ (X = Cl, Br, I) nanostructures for highly efficient photocatalytic applications. *Nanoscale* **2014**, *6*, 2009–2026. [CrossRef]
11. Liu, W.L.; Li, Q.; Yang, X.L.; Chen, X.F.; Xu, X.G. Synthesis of SiC/BiOCl composites and its efficient photocatalytic activity. *Catalysts* **2020**, *10*, 946. [CrossRef]
12. Ding, L.; Wei, R.; Chen, H.; Hu, J.; Li, J. Controllable synthesis of highly active BiOCl hierarchical microsphere self-assembled by nanosheets with tunable thickness. *Appl. Catal. B-Environ.* **2015**, *172*, 91–99. [CrossRef]
13. Li, Z.; Qu, Y.; Hu, K.; Humayun, M.; Chen, S.; Jing, L. Improved photoelectrocatalytic activities of BiOCl with high stability for water oxidation and MO degradation by coupling RGO and modifying phosphate groups to prolong carrier lifetime. *Appl. Catal. B-Environ.* **2017**, *203*, 355–362. [CrossRef]
14. Guo, L.; Han, X.X.; Zhang, K.L.; Zhang, Y.Y.; Zhao, Q.; Wang, D.J.; Fu, F. In-situ construction of 2D/2D ZnIn$_2$S$_4$/BiOCl heterostructure with enhanced photocatalytic activity for N$_2$ fixation and phenol degradation. *Catalysts* **2019**, *9*, 729. [CrossRef]
15. Liu, Y.Z.; Xu, J.; Wang, L.Q.; Zhang, H.Y.; Xu, P.; Duan, X.G.; Sun, H.Q.; Wang, S.B. Three-diemensional BiOI/BiO$_X$ (X = Cl or Br) nanohybrids for enhanced visible-light photocatalytic activity. *Nanomaterials* **2017**, *7*, 64. [CrossRef]
16. Li, S.J.; Hu, S.W.; Xu, K.B.; Jiang, W.; Liu, J.S.; Wang, Z.H. A novel heterostructure of BiOI nanosheets anchored onto MWCNTs with excellent visible-light photocatalytic activity. *Nanomaterials* **2017**, *7*, 22. [CrossRef]
17. Jiang, J.; Zhang, X.; Sun, P.; Zhang, L. ZnO/BiOI Heterostructures: Photoinduced charge-transfer property and enhanced visiblelight photocatalytic activity. *J. Phys. Chem. C* **2011**, *115*, 20555–20564. [CrossRef]
18. Wang, X.J.; Yang, W.Y.; Li, F.T.; Zhao, J.; Liu, R.H.; Liu, S.J.; Li, B. Construction of amorphous TiO$_2$/BiOBr heterojunctions via facets coupling for enhanced photocatalytic activity. *J. Hazard. Mater.* **2015**, *292*, 126–136. [CrossRef]
19. Viruthagiri, G.; Kannan, P. Visible light mediated photocatalytic activity of cobalt doped Bi$_2$O$_3$ nanoparticles. *J. Mater. Res. Technol.* **2019**, *8*, 127–133. [CrossRef]
20. Sheng, H.; Wang, W.; Dai, R.; Ning, J.; Zhang, L.; Wu, Q.; Zhang, F.C.; Yan, J.F.; Zhang, W.B. New insight into Cd^{2+}/Fe^{3+} co-doped BiOBr for enhancing the photocatalysis efficiency of dye decompositon under visible-light. *Nanomaterials* **2021**, *11*, 423. [CrossRef]
21. Sun, X.; Zhang, Y.; Li, C.; Zhang, Z.; Peng, Z.; Si, H.; Zhang, J.M.; Li, Y.T. BiOCl$_x$Br$_y$I$_z$ (x+y+z=1) solid solutions with controllable band gap and highly enhanced visible light photocatalytic performances. *J. Alloys Compd.* **2015**, *638*, 254–260. [CrossRef]
22. Kim, W.J.; Pradhan, D.; Min, B.K.; Sohn, Y. Adsorption/photocatalytic activity and fundamental natures of BiOCl and BiOCl$_x$I$_{1-x}$ prepared in water and ethylene glycol environments, and Ag and Au-doping effects. *Appl. Catal. B-Environ.* **2014**, *147*, 711–725. [CrossRef]
23. Zhang, J.; Wang, Z.W.; Fan, M.G.; Tong, P.P.; Sun, J.Y.; Dong, S.Y.; Sun, J.H. Ultra-light and compressible 3D BiOCl/RGO aerogel with enriched synergistic effect of adsorption and photocatalytic degradation of oxytetracycline. *J. Mater. Res. Technol.* **2019**, *8*, 4577–4587. [CrossRef]
24. Jiang, J.; Zhang, L.; Li, H.; He, W.; Yin, J.J. Self-doping and surface plasmon modification induced visible light photocatalysis of BiOCl. *Nanoscale* **2013**, *5*, 10573–10581. [CrossRef] [PubMed]
25. Xia, J.X.; Xu, L.; Zhang, J.; Yin, S.; Li, H.M.; Xu, H.; Di, J. Improved visible light photocatalytic properties of Fe/BiOCl microspheres synthesized via self-doped reactable ionic liquids. *Cryst. Eng. Commun.* **2013**, *15*, 10132–10141. [CrossRef]
26. Mi, Y.; Wen, L.Y.; Wang, Z.J.; Cao, D.W.; Xu, R.; Fang, Y.G.; Zhou, Y.L.; Lei, Y. Fe(III) modified BiOCl ultrathin nanosheet towards high-efficient visible-light photocatalyst. *Nano Energy* **2016**, *30*, 109–117. [CrossRef]
27. Huang, C.J.; Hua, J.L.; Cong, S.; Zhao, Z.G.; Qiu, X.Q. Hierarchical BiOCl microflowers with improved visiblelight-driven photocatalytic activity by Fe(III) modification. *Appl. Catal. B* **2015**, *174–175*, 105–112. [CrossRef]

28. Cui, J.; Tao, S.S.; Yang, X.L.; Yu, X.J.; Sun, S.D.; Yang, Q.; Wei, W.; Liang, S.H. Facile construction of nickel-doped hierarchical BiOCl architectures for enhanced visible-light-driven photocatalytic activities. *Mater. Res. Bull.* **2021**, *138*, 111208. [CrossRef]

29. Di, J.; Xia, J.X.; Yin, S.; Xu, H.; Xu, L.; Xu, Y.G.; He, M.Q.; Li, H.M. One-pot solvothermal synthesis of Cu-modified BiOCl via a Cu-containing ionic liquid and its visible-light photocatalytic properties. *RSC Adv* **2014**, *4*, 14281–14290. [CrossRef]

30. Pare, B.; Sarwan, B.; Jonnalagadda, S.B. Photocatalytic mineralization study of malachite green on the surface of Mn-doped BiOCl activated by visible light under ambient condition. *Appl. Surf. Sci.* **2011**, *258*, 247–253. [CrossRef]

31. Li, W.T.; Huang, W.Z.; Zhou, H.; Yin, H.Y.; Zheng, Y.F.; Song, X.C.S. Synthesis of Zn^{2+} doped BiOCl hierarchical nanostructures and their exceptional visible light photocatalytic properties. *J. Alloys Compd.* **2015**, *638*, 148–154. [CrossRef]

32. Yang, J.; Liang, Y.J.; Li, K.; Yang, G.; Zhu, Y.L.; Liu, S.Q.; Lei, W. New reaction pathway induced by the synergistic effects of Bi plasmon and La^{3+} doping for efficient visible light photocatalytic reaction on BiOCl. *Appl. Surf. Sci.* **2018**, *458*, 769–780. [CrossRef]

33. Jia, T.K.; Liu, M.; Zheng, C.Y.; Long, F.; Min, Z.Y.; Fu, F.; Yu, D.S.; Li, J.L.; Lee, J.H.; Kim, N.H. One-pot hydrothermal synthesis of la-doped $ZnIn_2S_4$ microspheres with improved visible-light photocatalytic performance. *Nanomaterials* **2021**, *10*, 2026. [CrossRef] [PubMed]

34. Feng, H.N.; Xu, D.Y.; Wang, Q.W.; Dong, Y.L.; Zhang, G.M.; Lv, L.Y.; Ren, Z.J.; Wang, P.F.; Campos, L.C. Enhancement of superoxide evolution by nickel-doped for the removal of organic pollutants and cyanobacteria. *J. Taiwan Inst. Chem. Eng.* **2020**, *113*, 396–405. [CrossRef]

35. Chen, J.C.; Yu, C.L.; Li, J.D.; Fang, W.; He, H.B. Preparation by grinding-calcination and photocatalytic performance of La_2O_3/BiOCl composite photocatalysts. *J. Inorg. Mater.* **2015**, *30*, 943–949.

36. Xu, K.K.; Fu, X.L.; Peng, Z.J. Facile synthesis and photocatalytic activity of La-doped BiOCl hierarchical, flower-like nano-/microstructures. *Mater. Res. Bull.* **2017**, *98*, 103–110. [CrossRef]

37. Yu, N.; Chen, Y.; Zhang, W.H.; Wen, M.; Zhang, L.S.; Chen, Z.G. Preparation of Yb^{3+}/Er^{3+} co-doped BiOCl sheets as efficient visible-light-driven photocatalysts. *Mater. Lett.* **2016**, *179*, 154–157. [CrossRef]

38. Niu, S.Y.; Zhang, R.Y.; Zhou, X.J.; Zhao, X.Q.; Suo, H.; Jiao, Y.; Yao, H.B.; Guo, C.F. The enhanced photocatalytic activity of Yb3+-Ho^{3+}/Er^{3+} co-doped 3D BiOCl flower. *Dyes Pigments* **2018**, *149*, 462–469. [CrossRef]

39. Nussbaum, M.; Shaham-Waldmann, N.; Paz, Y. Synergistic photocatalytic effect in Fe,Nb-doped BiOCl. *J. Photochem. Photobiol. A* **2014**, *290*, 11–21. [CrossRef]

40. Zhong, Y.X.; Liu, Y.H.; Wu, S.; Zhu, Y.; Chen, H.B.; Yu, X.; Zhang, Y.M. Facile fabrication of BiOI/BiOCl immobilized films with improved visible light photocatalytic performance. *Front. Chem.* **2018**, *6*, 58. [CrossRef]

41. Shi, R.; Huang, G.; Lin, J.; Zhu, Y. Photocatalytic activity enhancement for Bi_2WO_6 by fluorine substitution. *J. Phys. Chem. C* **2009**, *113*, 19633–19638. [CrossRef]

42. Li, X.K.; Yang, J.; Zhang, W.J. Influence of tetrabutylammonium hydroxide on the microstructural, optical and photocatalytic properties of sol-gel derived $Gd_2Ti_2O_7$ for RBR X-3B degradation. *J. Mater. Res. Technol.* **2021**, *12*, 202–209. [CrossRef]

43. Lu, T.; Liu, G.; Li, C.X.; Zhang, W.T.; Fan, J.J.; Wu, L.S.; Liu, J.H. Photocatalytic degradation of methylene blue in water by $BiOCl/SiO_2/Fe_3O_4$ composites. *Acta Sci. Circumstantiae* **2019**, *39*, 352–358.

44. Lu, H.J.; Xu, L.L.; Wei, B.; Zhang, M.Y.; Gao, H.; Sun, W.J. Enhanced photosensitization process induced by the p-n junction of $Bi_2O_2CO_3$/BiOCl heterojunctions on the degradation of rhodamine B. *Appl. Surf. Sci.* **2014**, *303*, 360–366. [CrossRef]

45. Zhong, S.; Li, C.Y.; Shen, M.N.; Lv, C.; Zhang, S.Y. Synthesis of modified bismuth tungstate and the photocatlytic properties on tetracycline degradation and pathways. *J. Mater. Res. Technol.* **2019**, *8*, 1849–1858. [CrossRef]

46. Ai, Z.H.; Ho, W.K.; Lee, S.C. Efficient visible light photocatalytic removal of NO with BiOBr-graphene nanocomposites. *J. Phys. Chem. C* **2011**, *115*, 25330–25337. [CrossRef]

47. Shinde, N.M.; Xia, Q.X.; Yun, J.M.; Singh, S.; Mane, R.S.; Kim, K.H. A binder-free wet chemical synthesis approach to decorate nanoflowers of bismuth oxide on Ni-foam for fabricating laboratory scale potential pencil-type asymmetric supercapacitor device. *Dalton Trans.* **2017**, *46*, 6601–6611. [CrossRef]

48. Chen, P.; Chen, L.; Zeng, Y.; Ding, F.; Jinag, X.; Liu, N.; Au, C.T.; Yin, S.F. Three-dimension hierarchical heterostructure of $CdWO_4$ microrods decorated with Bi_2WO_6 nanoplates for high-selectivity photocatalytic benzene hydroxylation to phenol. *Appl. Catal. B Environ.* **2018**, *234*, 311–317. [CrossRef]

49. Meng, X.C.; Zhang, Z.S. New insight into BiOX (X = Cl, Br, and I) hierarchical microspheres in photocatalysis. *Mater. Lett.* **2018**, *225*, 152–156. [CrossRef]

50. Li, S.J.; Chen, J.L.; Hu, S.W.; Jiang, W.; Liu, Y.P.; Liu, J.S. Bi_2WO_6 and its excellent photocatalytic performance for the degradation of toxic pharmaceutical antibiotics. *Inorg. Chem. Front.* **2020**, *7*, 529–541. [CrossRef]

51. Nie, J.; Hassan, J.L.; Jia, Q.; Gao, Y.F.; Peng, J.Z.; Lu, J.H.; Zhang, F.C.; Zhu, G.Q.; Wang, Q.Z. La-doped $ZnWO_4$ nanorods with enhanced photocatalytic activity for NO removal: Effects of La doping and oxygen vacancies. *Inorg. Chem. Front.* **2020**, *7*, 356–368. [CrossRef]

52. Xiong, F.; Yin, L.-L.; Wang, Z.; Jin, Y.; Sun, G.; Gong, X.-Q.; Huang, W. Surface reconstruction-induced site-specific charge separation and photocatalytic reaction on anatase TiO_2 (001) surface. *J. Phys. Chem. C* **2017**, *121*, 9991–9999. [CrossRef]

53. Lv, Z.; Zhou, H.; Liu, H.; Liu, B.; Liang, M.; Guo, H. Controlled assemble of oxygen vacant CeO_2@ Bi_2WO_6 hollow magnetic microcapsule heterostructures for visible-light photocatalytic activity. *Chem. Eng. J.* **2017**, *330*, 1297–1305. [CrossRef]

54. Chinh, V.; Bavasso, I.; Palma, L.; Felici, A.; Scarsella, M.; Vilardi, G.; Bracciale, M.; Van, N. Enhancing the photocatalytic activity of TiO_2 and TiO_2-SiO_2 by coupling with graphene-gold nanocomposites. *J. Mater. Sci. Mater. Electron.* **2021**, *32*, 5082–5093. [CrossRef]

55. Liang, S.J.; Zhu, S.Y.; Chen, Y.; Wu, W.M.; Wang, X.C.; Wu, L. Rapid template-free synthesis and photocatalytic performance of visible light-activated $SnNb_2O_6$ nanosheets. *J. Mater. Chem.* **2012**, *22*, 2670–2678. [CrossRef]

56. Qiao, Q.; Huang, W.Q.; Li, Y.Y.; Li, B.; Hu, W.; Peng, W.; Fan, X.; Huang, G.F. In-situ construction of 2D direct Z-scheme g-C_3N_4/g-C_3N_4 homojunction with high photocatalytic activity. *J. Mater. Sci.* **2018**, *53*, 15882–15894. [CrossRef]

57. Cao, Q.W.; Zheng, Y.F.; Song, X.C. Enhanced visible-light-driven photocatalytic degradation of RhB by $AgIO_3$/WO_3 composites. *J. Taiwan Inst. Chem. Eng.* **2017**, *70*, 359–365. [CrossRef]

58. Liu, Y.B.; Zhu, G.Q.; Gao, J.Z.; Hojamberdiev, M.; Zhu, R.L.; Wei, X.M.; Guo, Q.M.; Liu, P. Enhanced photocatalytic activity of Bi4Ti3O12 nanosheets by Fe^{3+}-doping and the addition of Au nanoparticles: Photodegradation of phenol and bisphenol A. *Appl. Catal. B-Environ.* **2017**, *200*, 72–82. [CrossRef]

59. Achola, L.A.; Ghevrehiwet, A.; Macharia, J.; Kerns, P.; He, J.; Fee, J.; Tinson, C.; Shi, J.; March, S.; Jain, M.; et al. Enhanced visible-light-assisted peroxymonosulfate activation on cobaltdoped mesoporous iron oxide for orange II degradation. *Appl. Catal. B* **2020**, *263*, 118332. [CrossRef]